Research paper

PolarBRDF: A general purpose Python package for visualization and quantitative analysis of multi-angular remote sensing measurements

Manoj K. Singh [a,*], Ritesh Gautam [a,b,**], Charles K. Gatebe [c,d,***], Rajesh Poudyal [e]

[a] Centre of Studies in Resources Engineering, Indian Institute of Technology Bombay, Mumbai 400076, India
[b] Interdisciplinary Program in Climate Studies, Indian Institute of Technology Bombay, Mumbai 400076, India
[c] Universities Space Research Association, Columbia, MD 21046, USA
[d] NASA Goddard Space Flight Center, Greenbelt, MD 20771, USA
[e] Science Systems and Applications, Inc, Lanham, MD, USA

A B S T R A C T

The Bidirectional Reflectance Distribution Function (BRDF) is a fundamental concept for characterizing the reflectance property of a surface, and helps in the analysis of remote sensing data from satellite, airborne and surface platforms. Multi-angular remote sensing measurements are required for the development and evaluation of BRDF models for improved characterization of surface properties. However, multi-angular data and the associated BRDF models are typically multidimensional involving multi-angular and multi-wavelength information. Effective visualization of such complex multidimensional measurements for different wavelength combinations is presently somewhat lacking in the literature, and could serve as a potentially useful research and teaching tool in aiding both interpretation and analysis of BRDF measurements. This article describes a newly developed software package in Python (*PolarBRDF*) to help visualize and analyze multi-angular data in polar and False Color Composite (FCC) forms. *PolarBRDF* also includes functionalities for computing important multi-angular reflectance/albedo parameters including spectral albedo, principal plane reflectance and spectral reflectance slope. Application of *PolarBRDF* is demonstrated using various case studies obtained from airborne multi-angular remote sensing measurements using NASA's Cloud Absorption Radiometer (CAR). Our visualization program also provides functionalities for untangling complex surface/atmosphere features embedded in pixel-based remote sensing measurements, such as the FCC imagery generation of BRDF measurements of grasslands in the presence of wildfire smoke and clouds. Furthermore, *PolarBRDF* also provides quantitative information of the angular distribution of scattered surface/atmosphere radiation, in the form of relevant BRDF variables such as sunglint, hotspot and scattering statistics.

© 2016 Elsevier Ltd. All rights reserved.

1. Introduction

The Earth's surface-atmosphere system is heterogeneous in nature, even at the scale of small particles in the atmosphere or canopy structure in a forest cover. Unless the surface is very smooth and mirror-like, the radiation reflected is inherently diffuse in nature. Furthermore, the position of the Sun (which is the source of illumination in passive remote sensing) varies significantly in the principal plane (the plane passing through the center of the sun-sensor geometry containing the Sun), which can influence the amount and behavior of light reflected from a surface. At any given observing instant, the radiance measured at the satellite, aircraft or at the surface level, depends on the Solar Zenith Angle (θ_0), Viewing Zenith Angle (θ) and Relative Azimuth Angle (ϕ), which together form the Sun-sensor geometry. For example, at a smaller θ, reflectance due to scattering by pollution particles in the atmosphere is relatively lower compared to larger θ due to enhanced scattering at larger θ associated with the longer optical path length. The Sun-sensor geometry together with the characteristics of surface produces an angular distribution of reflectance widely known as the Bidirectional Reflectance Distribution Function (BRDF) (Nicodemus et al., 1977). The BRDF is also widely used to describe light transport in computer vision and graphics (Blinn, 1977; Nishino and Lombardi, 2011; Phong, 1975; Schlick, 1994).

More technically, BRDF describes the angular distribution of

reflectance for a given point on a surface and is a function of θ_0, θ and ϕ. Multi-angular remote sensing has enabled BRDF characterization of various surface types and atmospheric features including ocean, vegetation, snow, desert, wetlands, cloud decks, smoke layers (Gatebe and King, 2016). In this paper, we will use the conventional definition of BRDF as the basic parameter for describing (geometrically) the reflecting properties of a surface element, while the Bidirectional Reflectance Factor (BRF), or simply the reflectance, is a non-dimensional quantity equivalent to BRDF multiplied by π, which shows quickly the difference between the measured surface and a Lambertian reflector (Gatebe and King, 2016). The characterization and understanding of BRDF is important for producing remote sensing-based retrievals of geophysical parameters as shown in several studies (e.g. Ahmad and Deering, 1992; Loeb et al., 2003, 2005; Patadia et al., 2011; Su et al., 2015). Additionally, Longbotham et al. (2012) showed that there is significant improvement in classification accuracy available from multiangle WorldView-2 sequence of images. In another land-use classification study, Koukal and Atzberger (2012) demonstrated that multi-angular data effectively discriminates between different forest types with better accuracy, as compared to the sole use of spectral information.

Given the importance of BRDF and multi-angular remote sensing, the interpretation of visual information becomes important for improved analysis of surface characterization. Polar plots provide a convenient way to visualize multi-angular data, either spectrally or via different band combinations. Effective visualization of BRDF data in a polar form can aid in deriving important properties about the type of surface and the overlaying atmospheric composition. This article describes a new software package (*PolarBRDF*) for use by the remote sensing community in analyzing visual and statistical information about multi-angular remote sensing data. *PolarBRDF* is a freely available tool developed in Python, which is a leading open source general purpose, high-level programming language, widely used by the scientific community.

Salient features and functionalities of *PolarBRDF* include the extraction of BRDF information along any given θ or ϕ, for the analysis of angular distribution of scattered radiation for various types of surface/atmospheric features. For example, it can be readily used for extracting information along the solar principal plane relevant for the characterization of sunglint and hotspot phenomena. The "hotspot" over vegetated surfaces is associated with enhancement of reflection in the antisolar direction, where the sun is located directly behind the sensor (Gatebe and King, 2016). The new software allows quick extraction of data from any scattering plane, including forward and backward scattering planes. This package also provides plotting of multi-angular data in polar form. One of the main features is the visualization of multi-angular data via True/False-Color-Composite (FCC) imagery using a combination of selected channels. In addition, *PolarBRDF* provides spectral analysis of multi-channel angular dataset at different spectral channels. The utility and application of *PolarBRDF* functionalities have recently been demonstrated in studies dealing with multi-angular remote sensing measurements from the Cloud Absorption Radiometer (CAR). The optical features of various surface types including sunglint over water bodies, hotspot over vegetation, glory and cloud-bow for liquid water clouds, were described and visualized recently using PolarBRDF (Gatebe and King, 2016). Additionally, Gautam et al. (2016) used *PolarBRDF* and CAR measurements for characterizing the radiative properties of clouds embedded in smoke. The following sections describe the methodology and application of the software to multi-angular remote sensing measurements, relating to visualization and analysis obtained from *PolarBRDF*. An appendix section is also included in the supplementary material describing the input-output and usage functionalities of *PolarBRDF*.

2. Methodology and data

In this paper, we use multi-angular remote sensing measurements obtained with NASA's airborne Cloud Absorption Radiometer (CAR, http://car.gsfc.nasa.gov/) as a testbed to demonstrate the visualization and analysis functionalities of *PolarBRDF*. The CAR is a multi-wavelength scanning radiometer that was originally designed and built in 1983 as a 13-channel scanning radiometer (King et al., 1986). The instrument was subsequently upgraded to a 14-channel radiometer in 2000, consisting of these channels- 0.34 μm, 0.38 μm, 0.47 μm, 0.68 μm, 0.87 μm, 1.04 μm, 1.22 μm, 1.27 μm; one out of 1.56 μm, 1.66 μm, 1.74 μm, 2.10 μm, 2.20 μm and 2.30 μm (Gatebe et al., 2003). We used CAR measurements over various surface types and environmental regimes from several airborne campaigns. These include data from the Arctic Research of the Composition of the Troposphere from Aircraft and Satellites (ARCTAS) (flight #2016 and #2017) and Smoke/Sulfates Clouds and Radiation - Brazil (SCAR-B) (flight #1701). The ARCTAS flight #2017 includes measurements during a vertical profile in the most homogeneous part of the biomass burning smoke plume and an across-plume low-level leg in Saskatchewan, Canada. More details about the CAR instrument and acquired data over different surfaces can be found in Arnold et al. (2002), Gatebe and King (2016), Gatebe et al. (2003, 2005), Georgiev et al. (2009), King et al. (1986), Lyapustin et al. (2010), Roman et al. (2011), and Tsay et al. (1998).

In mathematical literature, polar data are described in terms of r and θ. Since our objective is the visualization/analysis of BRF data, we will use the convention of θ and ϕ. In our polar plots, θ is 0° at the center and monotonically increases towards the periphery to 90°. In other words, θ measures the radial distance from the center. At any point in the polar plot, ϕ (relative azimuth angle) is the angle between the lines joining the point and the northern tip of the plot (both lines originating at the center of the polar plot), along the clockwise direction. An azimuth of 0° (or 360°) represents forward scattering, while 180° represents backward scattering (Gatebe and King, 2016). Here, the aircraft carrying the CAR makes a complete circle where the sensor continuously scans across track from zenith to horizon to nadir. We only show the CAR-derived reflectance data mapped onto the plot plots, corresponding to the horizon-to-nadir coverage. The position of the aircraft is located at the center of the polar plot, where the aircraft makes a complete circular transect within a span of ∼2–3 min (Gatebe and King, 2016).

Multi-angular data can be visualized in rectangular/Cartesian (Fig. 1a) and/or polar projection (Fig. 1c). In Fig. 1a, BRF at 0.87 μm from CAR flight #2016 is plotted in a rectangular form. Since CAR provides multi-angular measurements, projection onto a polar form is a natural way of visualizing multi-angular data such as from CAR (and other multi-angular satellite/airborne sensors), where measurements at $\phi = 0°$ and 360° align well with the viewing azimuth directions. Fig. 1c shows the same information as plotted in Fig. 1a, but projected in a polar form. Here, the reflectance for θ is along the radial direction from the center to periphery of the circle. Whereas, the reflectance for $\phi = 0$–360°, for a fixed θ, is along a concentric circle with a fixed radius from the center of the circle.

Polar plots can either be generated for a single channel (Fig. 1c) or for a combination of spectral channels, referred to as FCC imagery (Fig. 1d). For example, Fig. 2 shows polar plots of reflectance from the CAR flight #2016 at four different channels: 0.34 μm, 0.47 μm, 0.87 μm and 1.22 μm. For all wavelengths, reflectance at smaller view angles is low, in general, compared to larger zenith angles, associated with a longer optical path length at larger view angles. The reflectance pattern is generally symmetric about the principal plane as the phase function of scattering is symmetric around this plane. Apart from these general features, at
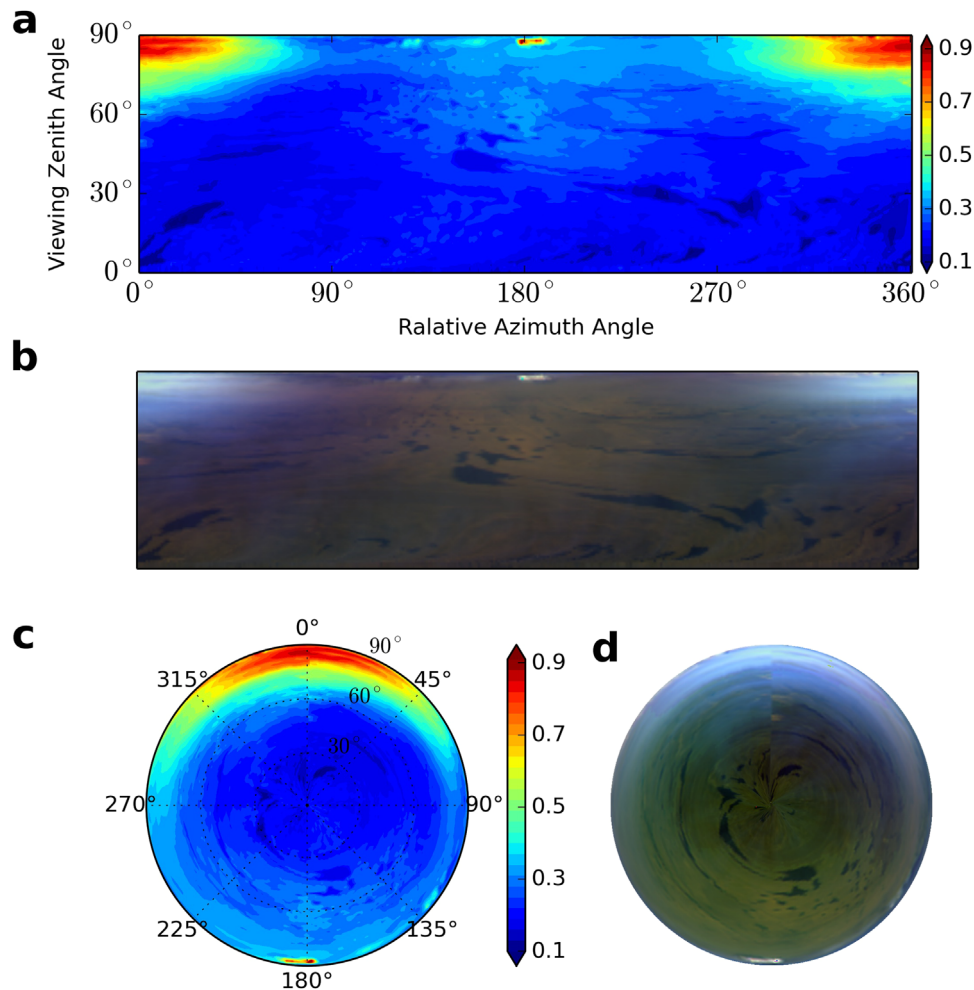
Fig. 1. Plots of reflectance measured by CAR during flight #2016 (30 June 2008) for viewing zenith angles within 0–90° and relative azimuth angle from 0° to 360° at an interval of 1°. (a) Rectangular plot at 0.87 μm, (b) rectangular False-color image formed by combining reflectance 1.04 μm as Red, 0.87 μm as Green and 0.47 μm as Blue. The white color indicates scattering due to smoke aerosols, whereas black denotes water bodies and green represents vegetation, (c) polar plot of reflectance at 0.87 μm and (d) False-color image formed by combining channel reflectances as defined in (b). (For interpretation of the references to color in this figure legend, the reader is referred to the web version of this article.)

0.34 μm (i.e. UV wavelength), the Rayleigh scattering is dominant where the reflectance pattern is symmetric, which is associated with similar magnitudes of forward and backward scattering. At 0.47 μm, scattering by smoke aerosols is dominant which is strongly forward scattering in nature; whereas in the near-IR wavelengths (e.g. 1.22 μm), surface features are more apparent as the influence of aerosol and Rayleigh scattering is minimal at longer wavelengths. Thus, it is convenient to visualize polar plots for different spectral channels, which provides useful information about the characteristics of both atmospheric and surface features.

FCC imagery can also be generated in *PolarBRDF* by combining reflectance at three bands and assigning them with three primary colors: Red, Green and Blue (RGB). Formation of an RGB image involves the following band and color selection criteria:

1. Band selection: Selection of three primary colors is based on the interest in highlighting various atmospheric/surface features in the resulting imagery. For example, in order to visualize a scene with smoke layer overlaying a given surface type; one channel should be greater than 1.00 μm, with the second between 0.6 μm to 0.8 μm (if the underlying surface is vegetated) and the third between 0.35 μm to 0.55 μm to represent scattering from smoke aerosols which is dominant in the UV–visible bands.
2. Color assignment scheme: A common false-color scheme for

optical remote sensing imagery is to assign short-wave infrared band with Red, near-infrared with Green and red band with Blue. The color selection can sometimes be feature-specific. For example, to detect the presence of smoke over vegetated surface in CAR data, bands which reflect the most for vegetation (e.g. 0.87 μm in the nearIR) can be assigned with Green. Whereas for other surface features, 1.04 μm can be assigned with Red while smoke can be assigned Blue color at 0.47 μm. In this kind of representation, water bodies will become naturally dark. Table 1 shows various combinations of channels which can be used to discriminate various optical features. Several of these combinations can be found in Gatebe and King (2016).

2.1. Implementation: PolarBRDF

Python is one of the leading open source and general purpose high-level programming languages, frequently used for analysis and visualization of scientific data (Hunter and Matplotlib, 2007; Oliphant, 2007; Tosi, 2009). *Matplotlib* (Hunter and Matplotlib, 2007) is a plotting library for Python to produce remarkable scientific plots. Several functions within *Matplotlib* such as *imshow*, *pcolor*, *pcolormesh* and *contourf* are used to plot contents of a matrix as images. We use *imshow* to visualize FCC images from data consisting of a three-dimensional array. The multi-angular
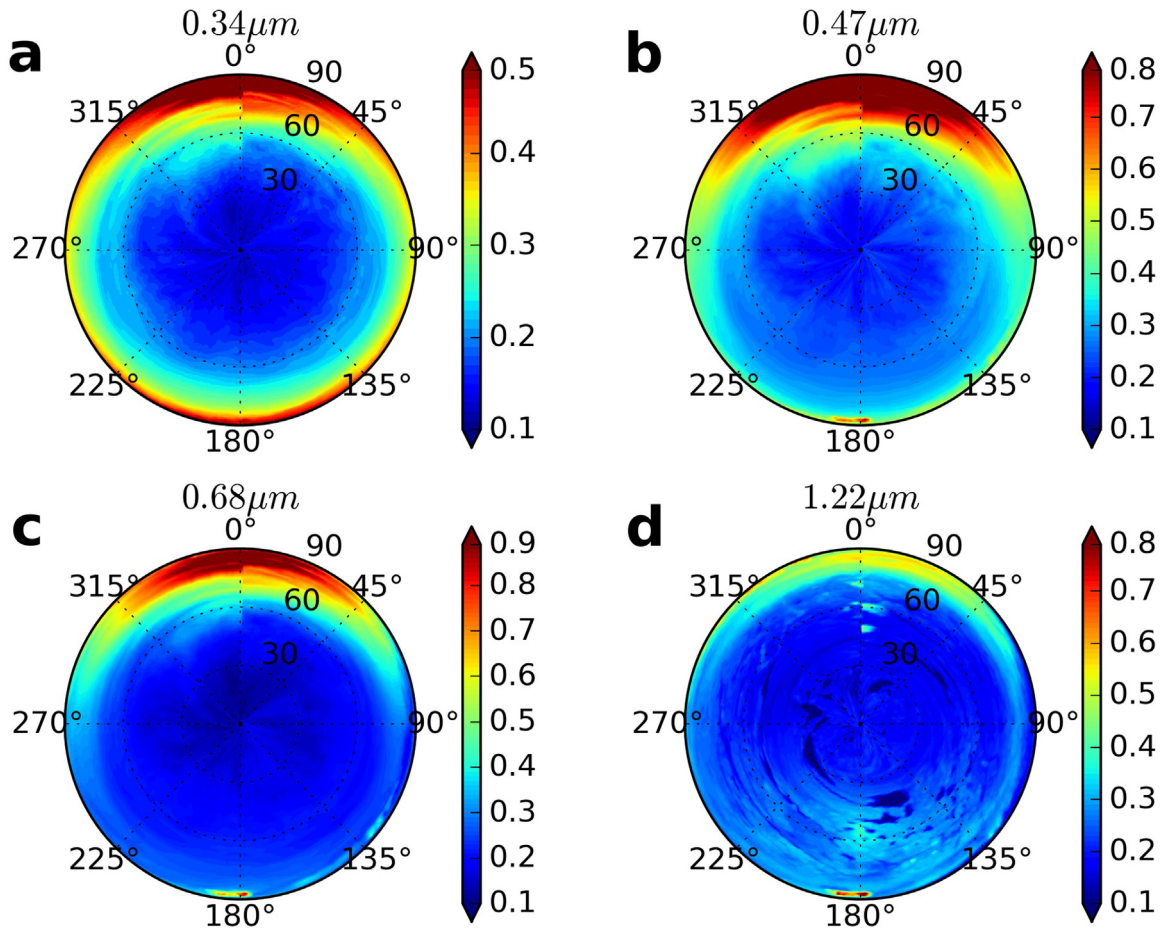
Fig. 2. Polar plot of surface reflectance measured by ARCTAS flight #2016 at (a) 0.34 μm, (b) 0.47 μm, (c) 0.68 μm and (d) 1.22 μm for viewing zenith angles within 0–90° and relative azimuth angle with 0–360° at an interval of 1°.

Table 1
The band combinations that may be used for discriminating various features (first column for Red, second for Green, third for Blue, and fourth for features discerned with the band combination).

Red (μm)	Green (μm)	Blue (μm)	Features
1.04	0.87	0.47	Ocean and Lakes, Clouds
1.04	0.87	0.47	Smoke, Forest fire
1.04	0.68	0.47	Forest, Cropland, Savanna, Mangroves
1.04	0.87	0.67	Desert, Salt pan

dataset from CAR measurements are three-dimensional arrays, consisting of θ, ϕ and band index. This three-dimensional dataset can be visualized using the default options of *imshow* in a rectangular plot (Fig. 1b).

The *imshow* function assumes the angular two-dimensional array of data as rectangular. Therefore, to visualize FCC polar image, the polar array must be converted to a Cartesian form. Assume $X(i, j)$ and $Y(i, j)$ are matrices of size 181 × 361 of Cartesian coordinates corresponding to 181 θ's (0–90°) and 361 ϕ's (0–360°) with $i = 0 \ldots, 181$ at an interval of one half degree and $j = 0, \ldots, 360$ at one degree interval. The *PolarBRDF* will create images at any given resolution for θ and ϕ. X and Y are given as,

$$X[i, j] = \theta[i] \times \cos(\phi[j]\pi/180) \tag{1}$$

$$Y[i, j] = \theta[i] \times \sin(\phi[j]\pi/180) \tag{2}$$

for $i = 0, \ldots, 180$ and $j = 0, \ldots, 360$.

For computational purposes, the two-dimensional matrix X and Y, together with corresponding angular data for the selected three bands, are converted to one-dimensional data. The following piece of Python code executes the transformation from polar to Cartesian coordinate system, as well as transformation from two-dimensional to one-dimensional data. Here, polar_data_first_band is a two-dimensional calibrated radiance dataset in Hierarchical Data Format (HDF), scaled in reflectance units, which is then transformed to one-dimensional (data_first_band). The first and second columns of the variable *XY_one_d* corresponds to X and Y, respectively.

```
nr=181 # Number of view zenith angles
nt=360 # Number of relative azimuth angles
xy_one_d=np.zeros((360*181,2))
data_first_band=np.zeros((360*181))
data_second_band=np.zeros((360*181))
data_third_band=np.zeros((360*181))
for i in range(0, nr):
for j in range(0, nt):
    k=i*nt+j
    XY_one_d[k,0]=r[i]*np.cos(j*np.pi/180)
    XY_one_d[k,1]=r[i]*np.sin(j*np.pi/180)
    data_first_band[k]=polar_data_first_band[i,j]
    data_second_band[k]=polar_data_second_band[i,j]
    data_third_band[k]=polar_data_third_band[i,j]
```

Since polar data are circular, it is convenient to use *imshow* for visualizing multi-angular reflectances contained within a square (a rectangle with minimum area which contains a circle is a square). The rectangular data, transformed from the polar form, are gridded into a square grid of size 720×720. The matrix X and Y together with the polar data, transformed to a Cartesian coordinate system, are part of this square grid. Again, since the computations are performed using a one-dimensional array, this 720×720 grid is transformed to a one-dimensional array. The following lines of Python code performs the above transformation,

```
one_d_grid=np.zeros((720*720,2))
for i in range(0,720):
 for j in range(0,720):
  k=i*720+j
  one_d_grid[k,0]=two_d_grid_x[i]
  one_d_grid[k,1]=two_d_grid_y[j]
```

For visualization purpose, rectangular grids (stored as one-dimensional grid for computational purpose) are used in *PolarBRDF*. However, since the polar dataset is transformed from Cartesian to polar (using Eqs. (1) and (2)), it is not possible to associate each square grid with a polar grid. Therefore, many pixels in the square grid have invalid data. To fill these pixels, we used the cubic interpolation method for each band. The *griddata* function in Python's *scipy* library was used for cubic interpolation as shown below,

```
from scipy.interpolate import griddata
band1_1d=griddata(XY_one_d, data_first_band, one_d_grid,
   method='cubic')
band2_1d=griddata(XY_one_d, data_second_band, one_d_-
   grid, method='cubic')
band3_1d=griddata(XY_one_d, data_third_band, one_d_grid,
   method='cubic')
for i in range(0,720):
   k1=i*720
```
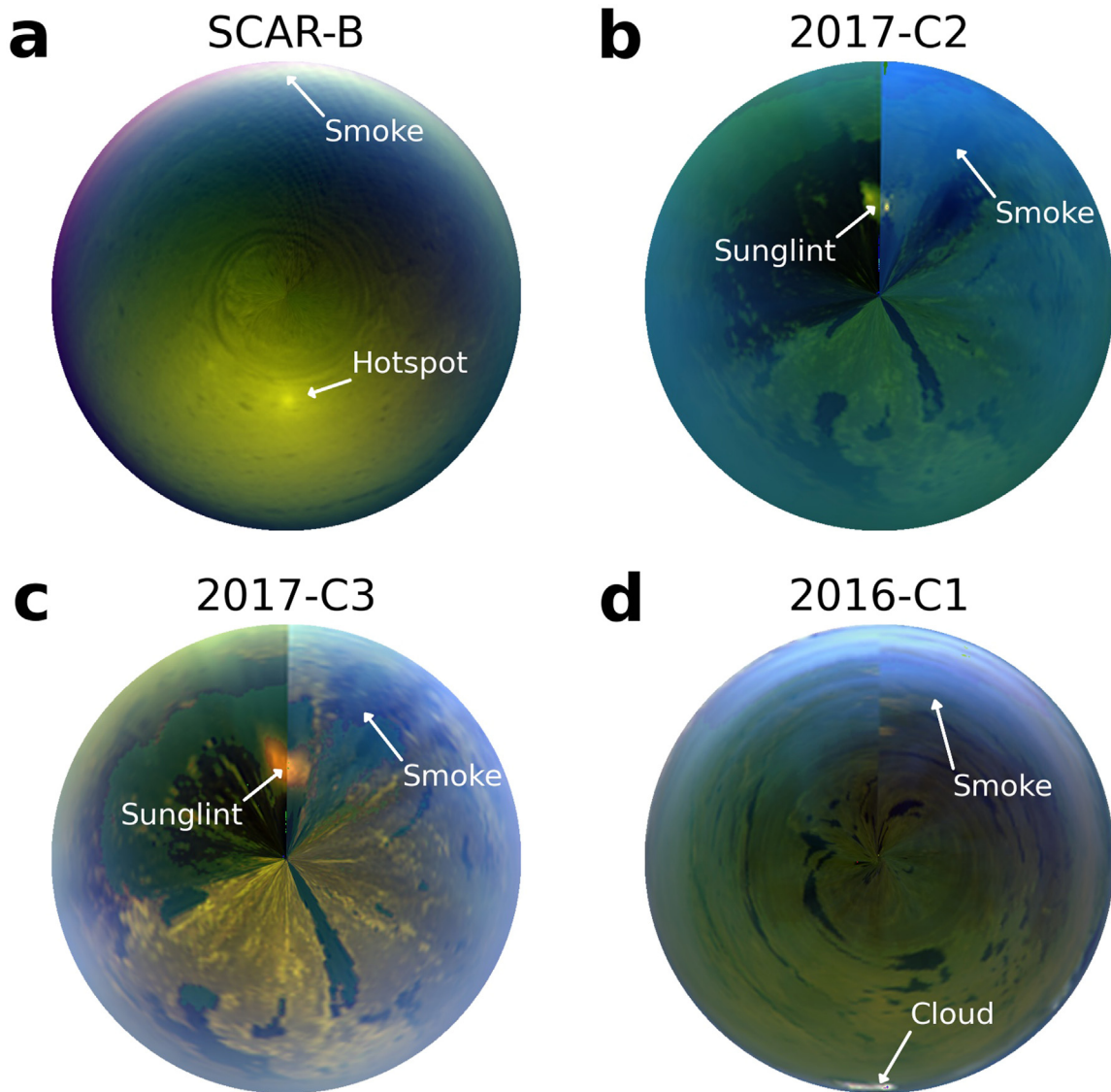

Fig. 3. Polar false-color images generated by *PolarBRDF* for surface reflectance measured from (a) SCAR-B flight #1701, ARCTAS flights (b) #2017-C2, (c) #2017-C3 and (d) #2016, by combining 1.04 μm as Red, 0.87 μm as Green and 0.47 μm as Blue. Note the presence of hotspot over vegetation in the backscattering direction (a), sunglint in the forward scattering (b and c), strong forward scattering of smoke, particularly at higher sensor zenith angles (all polar plots). (For interpretation of the references to color in this figure legend, the reader is referred to the web version of this article.)

```
k2=(i+1)*720
band1_2d[i,: ,0]=band1_1d[k1:k2]
band2_2d[i,: ,1]=band2_1d[k1:k2]
band3_2d[i,: ,2]=band3_1d[k1:k2]
```

Since the cubic interpolation function returns valid data only at points inside an approximated curvature-minimizing polynomial surface (approximately a circle in the cases used here), pixels outside the angular indices are invalid.

The variables *band1_2d, band2_2d* and *band3_2d* are in 720×720 square-gridded format for the angular data at the three selected bands. The reflectance values are scaled between *0* and *1* for use in generating FCC images.

3. Application of PolarBRDF

3.1. Analysis of reflectance

Fig. 3 shows four different cases of FCC images, where the presence of smoke aerosols is easy to distinguish over surface features. The CAR measurements from the SCAR-B campaign were obtained over forested land cover where the hotspot over vegetation in the backward scattering domain is apparent (visible as bright feature in the lower half of the polar plot, Fig. 3a). In addition, for flight #2017 (2017-C2 and 2017-C3), the thick smoke plume is clearly visible in the first quadrant of the polar plot (top-right of Fig. 3b and c). Since the flight #2017 spiraled downwards while completing a circle, the concentration of smoke reduced during descent, hence the observed reduction in the intensity of smoke scattering (Fig. 3b and c). In Fig. 3b and c (2017-C2 and C3), the bright spot shows the presence of sunglint (seen as yellow hue), formed due to specular reflection over the lake water under the path of the flight. It is also noted here that the apparent hazy appearance is associated with the strong forward scattering of smoke (in the upper part of all polar plots, particularly at larger sensor zenith angles).

3.2. Albedo estimation

The estimation of albedo is important for the characterization of its role in energy balance models (Kustas et al., 1989) and enhancing the capabilities of weather/climate modeling (Dickinson et al., 1990; Lean and Rowntree, 1997). The spectral albedo r_λ can be computed from BRDF, by integrating the reflection function over all solid angles (Tsay et al., 1998). i.e.

$$r_\lambda = \frac{1}{\pi} \int_0^{2\pi} \int_0^{\pi/2} R_\lambda(\theta_0, \theta, \phi) \cos\theta \, \sin\theta \, d\theta \, d\phi \tag{3}$$

For discrete number of ϕ and θ, Eq. (3) can be approximated with Eq. (4).

$$r_\lambda \cong 1/\mu_0 F_\lambda \sum_{i=1}^M \sum_{j=1}^N I_\lambda(\theta_0, \theta, \phi) \cos\theta_i \, \sin\theta_i \, \Delta\theta_i \, \Delta\phi_j \tag{4}$$

where indices *i* and *j* run over *M* number of θ between 0–90° and *N* number of ϕ between 0–360°, respectively. Since the CAR can measure reflectance at high angular resolution of θ and ϕ, the accuracy of the computed albedo is high. In *PolarBRDF*, we have added functionality to compute the albedo from multi-angular reflectance data (at the aircraft level) using Eq. (4). Fig. 4 shows the albedo computed at the aircraft level for 4 different cases of multi-angular reflectance data.

It is found from Fig. 4 that for flight #2017 circles, as the altitude of the aircraft decreases, there is a reduction in the apparent albedo due to variation in the intensity of Rayleigh scattering
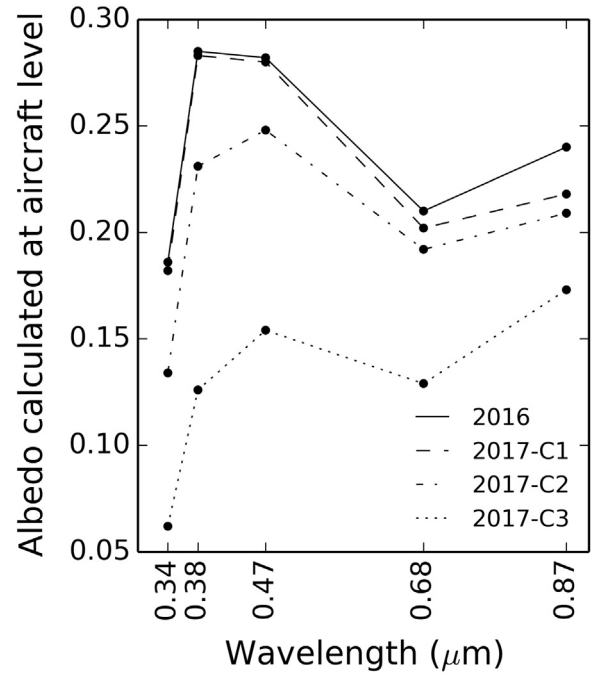

Fig. 4. Spectral Albedo computed at the aircraft level by *PolarBRDF* for ARCTAS flights #2016 (altitude ~5 km) and #2017 (descending from 3 km to 1.5 km) (three circles, 2017-C1, 2017-C2, 2017-C3) at five selected wavelengths.

(shallower atmosphere below the aircraft) and less scattering from smoke particles, especially for the shorter wavelengths. For similar reasons, flight #2016 shows higher albedo compared to flight #2017 as the altitude of flight #2016 (5 km) is higher than #2017 (3.0–1.5 km). The spectral albedo for the various channels (Fig. 4) also show that the intensity of smoke aerosol scattering is stronger compared to the Rayleigh scattering and the reflected radiation from vegetation. The input and output of the Python scripts for computation of spectral albedo are provided in the Appendix section (Supplementary Material).

3.3. Principal plane

In the polar plots shown in Fig. 2, reflectance along the principal plane is given by a line which bisects the plot in two equal left and right halves. Reflectance variation along the principal plane provides information about specular reflection and the hotspot, as well as the scattering nature of the surface (forward vs. backward scattering). *PolarBRDF* includes a Python script to extract reflectance along the principal plane. Fig. 5 shows the angular distribution of reflectance in the principal plane for measurements taken from ARCTAS flights #2016, #2017-C2&C3 and SCAR-B flight #1701 (reflectance at 0.47 μm over smoke). Higher reflectance in the upper quadrants of the polar plot indicates strong forward scattering of smoke aerosols, particularly observed at larger sensor zenith angles (seen previously in all polar plots in Fig. 3a–d). The apparent discontinuity in reflectance at 0° for flight #2017 is due to the spiraling descent of the aircraft. Whereas, during the SCAR-B measurements, the aircraft made circular measurements at the same altitude (and did not descend). Therefore during SCAR-B, there is no observed discontinuity. The scattering from smoke plumes is dominant at shorter wavelengths (e.g. 0.47 μm), as the reflectance from the underlying surface is low associated with the presence of water and vegetation.
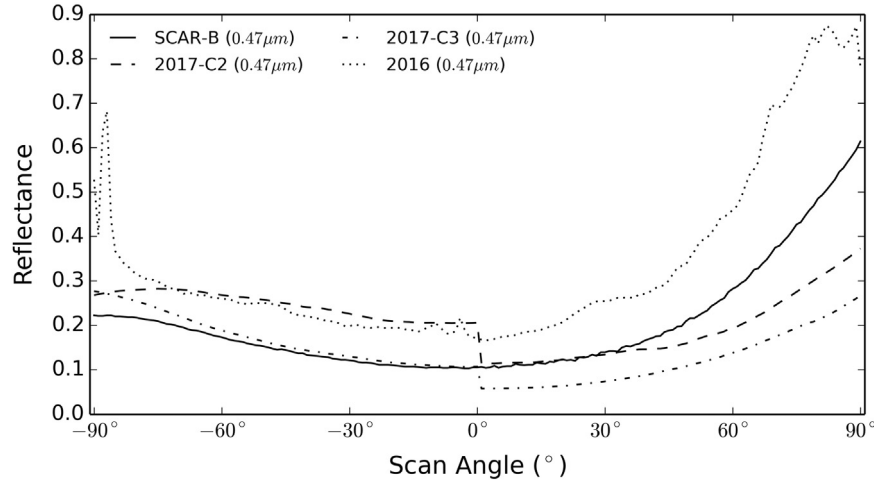
Fig. 5. Angular distribution of bidirectional reflectance function along the principal plane for measurements taken from flights #1701 (SCAR-B), #2016, #2017-circle-2, #2017-circle-3 (reflectance at 0.47 μm over smoke). Negative scan angles denote backward scattering direction and positive scan angles denote forward scattering direction. Discontinuity in the reflectance at 0° for #2017-C2 and C3 is due to the downward descent of the flight in spiraling mode.
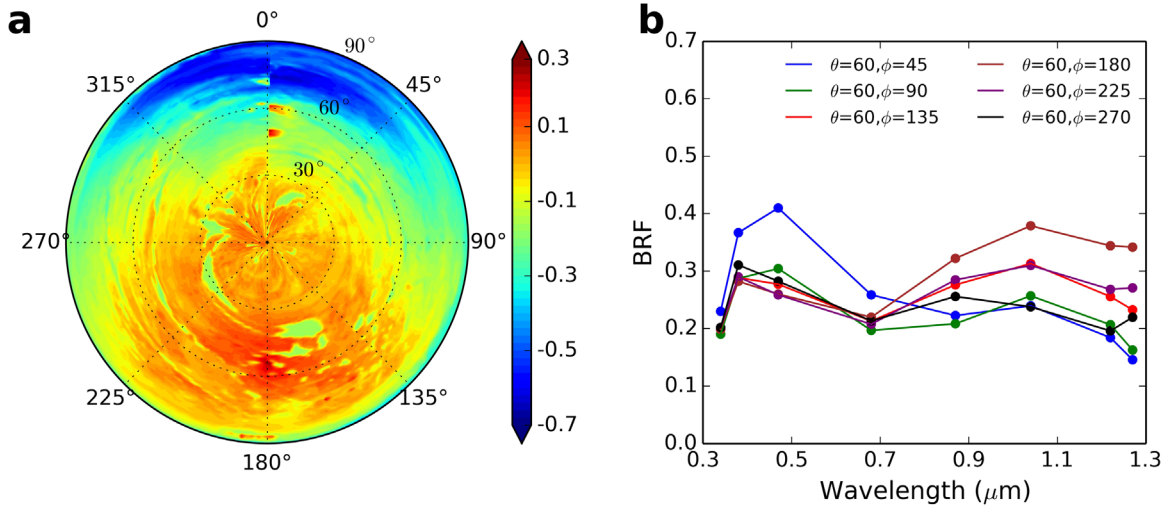

Fig. 6. (a) Spectral slope of reflectance for flight #2016 measurements computed from channels 0.47 μm, 0.68 μm, 0.87 μm, 1.04 μm, 1.22 μm, 1.27 μm and 1.66 μm. (**b**) Bidirectional Reflectance Function (BRF) from flight #2016 for wavelengths 0.34 μm, 0.38 μm 0.47 μm, 0.68 μm, 0.87 μm, 1.04 μm, 1.22 μm, 1.27 μm and 1.66 μm, at selected θ and ϕ (in deg) shown in the legend. (For interpretation of the references to color in this figure, the reader is referred to the web version of this article.)

3.4. Spectral Slope

We have also included a functionality in *PolarBRDF* for the calculation of the spectral slope of reflectance, which can be used to characterize different surface/atmospheric features. The spectral slope of reflectance is defined as the rate of change in reflectance with respect to wavelength, at a given θ and ϕ. Fig. 6a shows polar plot of spectral slope of reflectance with respect to wavelengths 0.47 μm, 0.68 μm, 0.87 μm, 1.04 μm, 1.22 μm, 1.27 μm and 1.66 μm, computed for flight #2016 from CAR's surface measurements. Corresponding to the FCC imagery shown Fig. 1, positive values in warm colors in the spectral slope polar plot (Fig. 6a) indicate the presence of vegetation due to higher reflectance in the near-IR compared to shorter visible wavelengths (e.g. 0.47 μm). Negative slope values (blue, or cold, colors) are indicative of cloud-free smoke-laden conditions (fine particles) in the forward scattering direction in the upper portion of the polar plot. The Python script also provides an extraction utility of spectral reflectance at any given θ and ϕ. For example, Fig. 6b shows line plots of reflectance at different combinations of θ and ϕ. Higher reflectances at 0.47 μm and low values at longer wavelengths (e.g. nearIR) indicates the presence of smoke, whereas the opposite pattern is

observed over a vegetated surface, as also seen in the earlier spectral slope polar plot. The analysis above suggests that FCC imagery provides useful visual information of the surface features and overlying atmospheric composition.

4. Summary and discussions

We have developed a software package by implementing a collection of Python scripts (*PolarBRDF*) to provide the remote sensing community an easy-to-use and effective tool for visualization and analysis of multi-angular remote sensing data, particularly related to the angular distribution of scattered radiation. The polar plot scripts provided with *PolarBRDF* aid in the visualization of multi-angular reflectances for the characterization of different surface and atmospheric features including grassland, cropland, snow, lake, ocean, clouds and smoke. *PolarBRDF* also provides functionality for visualizing False Color imagery further facilitating the characterization of surface/atmospheric features. Other basic BRDF variables along the principal plane can also be extracted to provide information about the presence and location of sunglint and hotspot. *PolarBRDF* also provides spectral slope maps of reflectance, indicating the presence

of clear-sky, cloudy-sky as well as smoke mixed with cloud. We have also added computations of some relevant statistics such as the spectral albedo, minimum, maximum and standard deviation of reflectances. In addition to its utility in research, we anticipate that *PolarBRDF* can also serve as a useful tool in teaching related to remote sensing.

Presently, *PolarBRDF* is specifically intended for measurements from multi-angular remote sensing measurements such as from CAR, but can be easily adapted to other similar sensors. Also, the software can be useful for many other satellite-derived measurements such as from MODIS, MISR, VIIRS, CERES and AVHRR, albeit in some restricted way. For instance, MODIS provides reflectance data in swath format. For a selected region, there is small variation in relative azimuth angle (ϕ) and view zenith angle (θ) in the sun-satellite geometry. Thus, a series of overlapping MODIS scenes over a selected region would allow a larger combination of ϕ and θ, for instance, to derive albedo information. Such approaches have been applied to the empirical development of angular distribution models (e.g. Patadia et al., 2011; Loeb et al., 2003). The analysis and visualization of reflectance calculated from well-known physical radiative transfer models such as Santa Barbara Disort Atmospheric Radiative Transfer (Ricchiazzi et al., 1998) and 3D radiation models (Iwabuchi, 2006; O`Hirok and Gautier, 1998) can also be carried out via *PolarBRDF*.

PolarBRDF is a first-of-its-kind tool, to our knowledge, developed for the analysis and visualization of multi-angular remote sensing measurements. Additionally, the advantage of *PolarBRDF* is that all the functionalities are built in Python, which is a freely-available and leading open-source Python programming language. This package is customized to accommodate the complexities associated with multi-angular BRDF data. Like any other newly-developed software, *PolarBRDF* also has some limitations. It takes input in a specific format; this will be expanded in future versions. *PolarBRDF* also assumes that the input dataset is on a regular grid for θ and ϕ. However, interpolation algorithms such as the cubic interpolation can be used to convert irregular to regular gridded data. *PolarBRDF* software along with sample examples will be made publically available at http://car.gsfc.nasa.gov/.

Acknowledgments

Appendix A. Supplementary material

Supplementary data associated with this article can be found in the online version at http://dx.doi.org/10.1016/j.cageo.2016.08.015.

References

Ahmad, S.P., Deering, D.W., 1992. A simple analytical function for bidirectional reflectance. J. Geophys. Res.: Atmos. 97 (D17), 18867–18886. http://dx.doi.org/10.1029/92JD01624.
Arnold, G.T., Tsay, S.-C., King, M.D., Li, J.Y., Soulen, P.F., 2002. Airborne spectral measurements of surface-atmosphere anisotropy for arctic sea ice and tundra. Int. J. Remote Sens. 23 (18), 3763–3781. http://dx.doi.org/10.1080/01431160110117373.
Blinn, J.F., 1977. Models of light reflection for computer synthesized pictures. SIGGRAPH Comput. Graph. 11 (2), 192–198. http://dx.doi.org/10.1145/965141.563893.
Dickinson, R.E., Pinty, B., Verstraete, M.M., 1990. Relating surface albedos in gcm to remotely sensed data. Agric. For. Meteorol. 52 (1), 109–131.
Gatebe, C.K., King, M.D., 2016. Airborne spectral BRDF of various surface types (ocean, vegetation, snow, desert, wetlands, cloud decks, smoke layers) for remote sensing applications. Remote Sens. Environ. 179, 131–148. http://dx.doi.org/10.1016/j.rse.2016.03.029.
Gatebe, C.K., King, M.D., Lyapustin, A.I., Arnold, G.T., Redemann, J., 2005. Airborne spectral measurements of ocean directional reflectance. J. Atmos. Sci. 62 (4), 1072–1092. http://dx.doi.org/10.1175/JAS3386.1.
Gatebe, C.K., King, M.D., Platnick, S., Arnold, G.T., Vermote, E.F., Schmid, B., 2003. Airborne spectral measurements of surface atmosphere anisotropy for several surfaces and ecosystems over southern Africa. J. Geophys. Res.: Atmos. 108 (D13), 8489. http://dx.doi.org/10.1029/2002JD002397.
Gautam, R., Gatebe, C.K., Singh, M.K., Varnai, T., Poudyal, R., 2016. Radiative characteristics of Clouds Embedded in Smoke derived from airborne multiangular measurements. J. Geophys. Res.: Atmospheres 121, 9140–9152. http://dx.doi.org/10.1002/2016JD025309.
Georgiev, G., Gatebe, C.K., Butler, J.J., King, M.D., 2009. BRDF analysis of savanna vegetation and salt-pan samples, Geoscience and Remote Sensing. IEEE Trans. 47 (8), 2546–2556. http://dx.doi.org/10.1109/TGRS.2009.2021331.
Hunter, J.D., Matplotlib, 2007. A 2d graphics environment. Comput. Sci. Eng. 9 (3), 90–95. http://dx.doi.org/10.1109/MCSE.2007.55.
Iwabuchi, H., 2006. Efficient Monte Carlo methods for radiative transfer modeling. J. Atmos. Sci. 63 (9), 2324–2339. http://dx.doi.org/10.1175/JAS3755.1.
King, M.D., Strange, M.G., Leone, P., Blaine, L.R., 1986. Multiwavelength scanning radiometer for airborne measurements of scattered radiation within clouds. J. Atmos. Ocean. Technol. 3 (3), 513–522. http://dx.doi.org/10.1175/1520-426.
Koukal, T., Atzberger, C., 2012. Potential of multi-angular data derived from a digital aerial frame camera for forest classification, Selected Topics in Applied Earth Observations and Remote Sensing. IEEE J. 5 (1), 30–43. http://dx.doi.org/10.1109/JSTARS.2012.2184527.
Kustas, W.P., Jackson, R.D., Asrar, G., 1989. Estimating surface energy-balance components from remotely sensed data. In: Asrar, G., (Ed.), Theory and Applications of Optical Remote Sensing. John Wiley, New York.
Lean, J., Rowntree, P.R., 1997. Understanding the sensitivity of a GCM simulation of Amazonian deforestation to the specification of vegetation and soil characteristics. J. Climate 10, 1216–1235. http://dx.doi.org/10.1175/1520-0442(1997)010<1216:UTSOAG>2.0.CO;2.
Loeb, N.G., Kato, S., Loukachine, K., Manalo-Smith, N., 2005. Angular distribution models for top-of-atmosphere radiative flux estimation from the clouds and the earth's radiant energy system instrument on the TERRA satellite. Part I: methodology. J. Atmos. Ocean. Technol. 22 (4), 338–351. http://dx.doi.org/10.1175/JTECH1712.1.
Loeb, N.G., Manalo-Smith, N., Kato, S., Miller, W.F., Gupta, S.K., Minnis, P., Wielicki, B.A., 2003. Angular distribution models for top-of-atmosphere radiative flux estimation from the clouds and the earth's radiant energy system instrument on the tropical rainfall measuring mission satellite. Part I: methodology. J. Appl. Meteorol. 42 (2), 240–265.
Longbotham, N., Chaapel, C., Bleiler, L., Padwick, C., Emery, W., Pacifici, F., 2012. Very high resolution multiangle urban classification analysis, geoscience and remote sensing. IEEE Trans. 50 (4), 1155–1170. http://dx.doi.org/10.1109/TGRS.2011.2165548.
Lyapustin, A., Gatebe, C.K., Kahn, R., Brandt, R., Redemann, J., Russell, P., King, M.D., Pedersen, C.A., Gerland, S., Poudyal, R., Marshak, A., Wang, Y., Schaaf, C., Hall, D., Kokhanovsky, A., 2010. Analysis of snow bidirectional reflectance from ARCTAS spring-2008 campaign. Atmos. Chem. Phys. 10 (9), 4359–4375. http://dx.doi.org/10.5194/acp-10-4359-2010.
Nicodemus, F.E., Richmond, J.C., Hsia, J.J., Ginsberg, I.W., Limperis, T., 1977. Ch. Geometrical Considerations and Nomenclature for Reflectance. Radiometry, Jones and Bartlett Publishers, Inc,, USA, pp. 94–145.
Nishino, K., Lombardi, S., 2011. Directional statistics-based reflectance model for isotropic bidirectional reflectance distribution functions. JOSA A 28 (1), 8–18.
O`Hirok, W., Gautier, C., 1998. A three-dimensional radiative transfer model to investigate the solar radiation within a cloudy atmosphere. Part I: spatial effects. J. Atmos. Sci. 55 (12), 2162–2179, http://dx.doi.org/10.1175/1520-0469(1998)055<2162:ATDRTM>2.0.CO;2.
Oliphant, T.E., 2007. Python for scientific computing. Comput. Sci. Eng. 9 (3), 10–20. http://dx.doi.org/10.1109/MCSE.2007.58.
Patadia, F., Christopher, S.A., Zhang, J., 2011. Development of empirical angular distribution models for smoke aerosols: methods. J. Geophys. Res.: Atmos. 116 (D14), d14203. http://dx.doi.org/10.1029/2010JD015033.
Phong, B.T., 1975. Illumination for computer generated pictures. Commun. ACM 18 (6), 311–317. http://dx.doi.org/10.1145/360825.360839.
Ricchiazzi, P., Yang, S., Gautier, C., Sowle, D., 1998. SBDART: a research and teaching software tool for plane-parallel radiative transfer in the earth's atmosphere. Bull. Am. Meteorol. Soc. 79 (10), 2101–2114, http://dx.doi.org/10.1175/1520-0477(1998)079<2101:SARATS>2.0.CO;2.
Roman, M.O., Gatebe, C.K., Schaaf, C.B., Poudyal, R., Wang, Z., King, M.D., 2011. Variability in surface BRDF at different spatial scales (30–500 m) over a mixed agricultural landscape as retrieved from airborne and satellite spectral measurements. Remote Sens. Environ. 115 (9), 2184–2203. http://dx.doi.org/10.1016/j.rse.2011.04.012.
Schlick, C., 1994. An inexpensive BRDF Model for physically-based rendering. Computer Graphics Forum 13, 233–246. http://dx.doi.org/10.1111/1467-8659.1330233.
Su, W., Corbett, J., Eitzen, Z., Liang, L., 2015. Next-generation angular distribution models for top-of-atmosphere radiative flux calculation from CERES instruments: methodology. Atmos. Meas. Technol. 8 (2), 611–632. http://dx.doi.org/10.5194/amt-8-611-2015.
Tosi, S., 2009. Matplotlib for Python Developers: Build Remarkable Publication Quality Plots the Easy Way. Packt Publishing Ltd, Birmingham, UK.
Tsay, S.-C., King, M.D., Arnold, G.T., Li, J.Y., 1998. Airborne spectral measurements of surface anisotropy during SCAR-B. J. Geophys. Res.: Atmos. 103 (D24), 31943–31953. http://dx.doi.org/10.1029/98JD01167.